A New Class of Solid Lewis Acid Catalysts Based on Interlayer Expansion of Layered Silicates of the RUB-36 Type with Heteroatoms

Trees De Baerdemaeker,[a] Hermann Gies,[b] Bilge Yilmaz,[c] Ulrich Müller,[d] Mathias Feyen,[d] Feng-Shou Xiao,[e] Weiping Zhang,[f] Toshiyuki Yokoi,[g] Xinhe Bao,[h] and Dirk E. De Vos*[a]

Interlayer expanded zeolites are derived from layered zeolite precursors by inserting a tetrahedrally coordinated atom (T-atom) in between the precursor layers. To achieve this expansion, a Si source like dichlorodimethylsilane or diethoxydimethylsilane is typically used. In the interlayer expansion of the layered zeolite precursor RUB-36, an Fe salt instead of a silylating agent was used to fill up the linking sites in between the layers. The obtained material showed a shift of the first XRD reflection similar to that of RUB-36 interlayer expanded with dichlorodimethylsilane, indicating an increase in interlayer distance. Diffuse reflectance UV-vis spectra and EPR characterization proved the incorporation of isolated Fe sites. Using FTIR spectroscopy with pyridine and acetonitrile as probe molecules, it was found that the incorporation of Fe results in an increase in Lewis acidity. The material was successfully used as a catalyst in the acylation of anisole with acetic anhydride and in the alkylation of toluene with benzyl chloride. The Fe incorporation proved to be remarkably stable. In spite of the HCl production during the alkylation reaction, no leaching was observed and the catalyst could be reused after regeneration.

Introduction

Zeolites are extensively applied as catalysts in the chemical industry.[1,2] They are crystalline, microporous (alumino)silicates consisting of a three-dimensional network of corner-sharing tetrahedra [TO_4] with several possibilities for isomorphous substitution of the central T-atom. The geometry and type of pore system of a zeolite as well as its chemical composition can have tremendous impact on the catalytic properties. This motivates the continuous search for new zeolite materials using various strategies, including insights from theoretical methods.[3-7] One of these strategies in developing new zeolite framework structures starts from layered zeolite precursors. Upon calcination, these materials undergo a topotactic condensation preserving the layer topology and resulting in crystalline, three-dimensional zeolites.[8-13] These layered materials can also be subjected to various post-synthesis modification treatments such as swelling, pillaring, delamination and recombination and, finally, interlayer expansion.[14-18] Via interlayer expansion, one extra T-atom is inserted in between the precursor layers, resulting in an increase of the pore size compared to the three-dimensional structure obtained through topotactic condensation.[19-21] This modification strategy can be seen as a way to create new zeolitic frameworks that cannot be obtained through direct synthesis and have their own distinct pore systems with functionalized linkers and corresponding catalytic properties.[4,14,22] For instance, in the case of the layered silicate RUB-36, Al could be incorporated in the layered precursor via direct synthesis. Interlayer expansion with a silylating agent like dichlorodimethylsilane (DCDMS) followed by calcination results in a zeolite named Al-COE-4. Its channel system consists of 10-membered ring (MR) pores as opposed to the 8-MR pores of the topotactic condensation product of RUB-36, RUB-37 (CDO topology). Through this interlayer expansion, a shape-selective zeolite catalyst for hydrocarbon conversion was obtained.[4,20]

Stimulated by the wide range of possibilities offered by the interlayer expansion concept, we investigated an alternative method to introduce and broaden catalytic functionalities

in layered silicates. In this contribution we demonstrate the first example of a novel methodology to obtain porous crystalline silicates containing transition metal heteroatoms via interlayer expansion. Heteroatom pillars are incorporated between (alumino)silicate layers, expanding the interlayer galleries. A wide variety of catalytically active centers can be incorporated into the zeolitic frameworks using this strategy by utilizing various metal precursors, paving the way to tailor-make catalysts for the specific needs of a reaction. The method is demonstrated here for the incorporation of isolated Fe sites. A post-synthesis modification treatment is applied to RUB-36 which is very similar to the aforementioned COE-4 synthesis procedure.[20] However, instead of using DCDMS, only an Fe salt is added to the layered precursor material with the objectiveto incorporate the Fe as isolated, catalytically active sites linking the layers of the zeolite precursor.[23] The obtained material, COE-4/Fe, was characterized and used as catalyst in the acylation of anisole with acetic anhydride and in the alkylation of toluene with benzyl chloride. The catalyst shows good crystallinity in the X-ray diffraction patterns, which allowed structure solution. Compared to *e.g.,* Fe_2O_3-loaded ZSM-5 obtained via incipient wetness impregnation, the incorporated iron is remarkably stable under the harsh alkylation reaction conditions.

Experimental

Catalyst synthesis

Purely siliceous and Al-containing RUB-36 were prepared according to previously published procedures.[4,20] The Si/Al ratio of the synthesis gel for Al-RUB-36 was 98, which resulted in Al-RUB-36 with Si/Al 100, proving near-complete Al incorporation. For the preparation of COE-4/Fe and Al-COE-4/Fe, the following procedure was used: 50 g 0.3 M HCl and 2.8 g of purely siliceous resp. Al-containing RUB-36 were placed in a Teflon cup and stirred for 10 min. 4.4 mmol $FeCl_3.6H_2O$ was added. The mixture was stirred for another 10 min after which the Teflon cup was closed and inserted in an autoclave. The mixture was treated hydrothermally for 24 h at 448 K under autogeneous pressure. The solids were recovered and washed with distilled water via filtration until the pH of the filtrate was neutral. The obtained solids were dried overnight at 393 K and then calcined at 773 K for 6 h (heating rate 1 K min^{-1}) resulting in a white powder. By analogy with the DCDMS expanded RUB-36, the Fe-containing materials before and after calcination are referred to as COE-3/Fe and COE-4/Fe, respectively, or Al-COE-3/Fe and Al-COE-4/Fe if Al-containing RUB-36 was used as precursor material. As reference material, Al-COE-4 was prepared following the procedure of Yilmaz *et al.*[4] A reference interlayer expansion treatment of RUB-36 using only 0.3 M HCl without the addition of any silylating agent or Fe salt was also performed. RUB-37 was obtained via calcination of the purely siliceous RUB-36 at 873 K for 4 h (heating rate 1 K min^{-1}). For comparison, a ZSM-5 sample (Süd-Chemie, H^+-form, Si/Al 80) was loaded with $Fe(NO_3)_3.9H_2O$ using the incipient wetness impregnation technique to obtain an Fe-loading that was similar to that of Al-COE-4/Fe. The preparation procedure was based on Choudary and Jana[24] and the experimental details can be found in the ESI.

Characterization

The X-ray diffraction analysis was carried out on the as-made sample COE-3/Fe. High resolution X-ray powder diffraction data were collected at room temperature with a Bruker D8 diffractometer operating in quasi Debye-Scherrer mode using monochromatized Mo Kα radiation (λ = 0.7106 Å). To prevent preferred orientation of the platelet sample, transmission geometry was used with capillary sample holders. Further details of the diffraction experiment are summarized in Table S1. Based on the indexed powder pattern, a structure model for COE-3/Fe was derived, adapted from the layered precursor RUB-36 and energy minimized using DLS[25] with geometric constraints on d(Si-O) = 1.60 Å, d(O-O) = 2.61 Å, and d(Si – Si) = 3.10 Å (Table

S1). Subsequently, the coordinates of the optimized tetrahedral network were used as starting parameters for the Rietveld refinement of the powder X-ray diffraction data using the FullProf-Suite of programs (χ^2 = 8.75).[26,27] A summary of the experimental parameters used and the results obtained from the Rietveld analysis including residuals and fractional coordinates are shown in Tables S1-3.

Other powder X-ray diffraction patterns (PXRD) were collected on a STOE Stadi MP diffractometer in Debye-Scherrer geometry with Cu Kα1 radiation (λ = 1.54056 Å), a linear position-sensitive detector (PSD) (6 °2θ window) and the sample in a capillary sample holder. Crystal size and morphology were determined using scanning electron microscopy (SEM) on a Philips XL30 FEG. Bulk elemental analysis was performed on a Varian Vista-PRO inductively coupled plasma optical emission spectrometer (ICP-OES). ^{29}Si MAS NMR spectra were collected on a 7.0 T Bruker AMX300 spectrometer (^{29}Si resonance frequency 59.6 MHz) using 4 mm zirconia rotors. Single pulse measurements were recorded using a recycle delay of 60 s, a pulse length of 5.0 µs, and a 5 kHz spinning frequency. Cross-polarization (CP) measurements used a 3 kHz spinning frequency, a 10 s recycle delay, a 5.0 µs ^{1}H 90° pulse, and a 5.0 ms contact pulse. To investigate the textural properties, N_2 physisorption isotherms were obtained at 77 K on a Micromeritics 3Flex Surface Characterization Analyzer. Prior to measurement, the samples were outgassed under vacuum at 473 K for 12 h. For comparison, the specific surface area was determined using the BET theory. The micropore volume was derived from *t*-plot analysis. X-band electron paramagnetic resonance (EPR) spectra were recorded at 116 K and 293 K on a Bruker ESP 300E instrument in a rectangular TE104 cavity (~9.6 GHz). The samples were measured both under ambient atmosphere in hydrated form and under N_2 atmosphere after drying at 473 K overnight. The different spectra were corrected for variations in frequency. UV-vis spectra between 200 and 800 nm were recorded under ambient atmosphere on a Varian Cary 5000 spectrometer in diffuse reflectance mode.

FTIR spectrometry was used to characterize the acidity using pyridine, acetonitrile and perdeuterated acetonitrile as probe molecules. IR spectra of self-supporting wafers of the zeolite samples (thickness 10-15 cm^2/g) were measured on a Nicolet 6700 FT-IR spectrometer with DTGS detector (128 scans, 2 cm^{-1} resolution). In case of pyridine adsorption, reference spectra were recorded at 423 K after heating under vacuum to 723 K for 1 h. Pyridine (25 mbar) was allowed to adsorb at 323 K and after saturation, the samples were evacuated for 30 min to remove the physisorbed pyridine before reheating (4 K/min) to 423 K and recording IR spectra of the samples containing chemisorbed pyridine. The number of acid sites was evaluated from the integral intensities of the absorption bands corresponding to pyridine adsorbed on Lewis (1450 cm^{-1}) and Brønsted acid sites (1545 cm^{-1}) using the molar extinction coefficients of Emeis.[28] When acetonitrile or perdeuterated acetonitrile were used as probe molecules, reference spectra were recorded at 298 K after heating under vacuum to 723 K for 1 h. The acetonitrile was allowed to adsorb at 298 K and after saturation, the samples were evacuated for 30 min before recording the IR spectra of the samples containing acetonitrile.

Catalytic experiments

Prior to reaction, all catalysts were dried at 473 K overnight. Acylation of anisole with acetic anhydride was carried out in glass crimp cap reactor vials loaded with 100 mg dried catalyst, 5.3 g anisole and 1 g acetic anhydride (molar ratio anisole/acetic anhydride 5) under N_2 atmosphere. The reactor vials were placed in a heated copper block at 363 K and stirred at 500 rpm.

Alkylation of toluene with benzylchloride was carried out in glass crimp cap reactors loaded with 100 mg catalyst and 7.8 mL dry toluene under N_2 atmosphere. A toluene/benzylchloride molar ratio of 10 was used. The reaction was carried out at 343 K. Reaction conditions were based on

Horcajada *et al.*[29] Samples (0.1 mL) were taken at regular intervals and analyzed on a Shimadzu 2010 GC equipped with a FID detector and a CP-Sil-5 column. Peaks were identified using authentic samples and GC-MS. To test the stability of the catalysts in the alkylation reaction, hot filtration tests were performed. At reaction temperature, the catalyst was removed from the reaction mixture by filtration and the filtrate was transferred quickly into a fresh reactor at reaction temperature. In another experiment, the Al-COE-4/Fe catalyst was recuperated after 24 h of reaction and calcined in air at 773 K for 4 h (heating rate 1 K min^{-1}) turning the green, used catalyst back into a white powder. The recycled catalyst was used in the same way as for the regular alkylation experiments but the experiment was performed on a smaller scale (35 mg catalyst). For comparison, the small scale reaction was also performed with the fresh Al-COE-4/Fe.

Results and discussion

Structure, morphology and chemical composition

Upon interlayer expansion of Al-RUB-36 with DCDMS, the first and most intense peak of the powder XRD pattern shifts to lower 2θ values (Fig. 1). This corresponds to a larger *d*-spacing (11.7 Å) than in the layered precursor (11.2 Å) and the calcined, condensed RUB-37 (Table 1). Replacing DCDMS by $FeCl_3.6H_2O$ in the interlayer expansion treatment of purely siliceous or Al-containing RUB-36 results in the materials COE-4/Fe and Al-COE-4/Fe, respectively. They both show a similar shift with a *d*-spacing of 11.7 Å (Fig. 1). Despite the large amount of Fe used, no Fe oxides were observed as precipitates in the reaction product, obviously because of the low pH and the high chloride concentration. SEM images of COE-4/Fe and Al-COE-4/Fe (Fig. 2) showed that the plate-like morphology of the layered precursor is preserved. In addition, no iron oxide particles were detected, indicating that the Fe must be present as a homogeneous constituent in the materials, either incorporated at isolated sites or intercalated in the form of very small clusters.

Table 1 Structural and textural properties of the COE-4-type materials

Sample	*d*-spacing (Å) [a]	BET area ($m^2\ g^{-1}$)	V_{micro} ($cm^3 g^{-1}$) [b]
RUB-36	11.2	34	<0.01
RUB-37	9.2	231	0.090
Al-COE-4	11.7	364	0.135
COE-4/Fe	11.7	423	0.156
Al-COE-4/Fe	11.7	389	0.136

[a] Derived from the first and most intense reflection in the PXRD pattern. [b] *t*-plot method.

Even though part of the Fe remained in solution, elemental analysis (Table 2) clearly indicates the presence of Fe in the Fe-expanded materials. For a defect-free purely siliceous COE-4 material, the chemical formula is $[Si_{20}O_{38}(OH)_4]$,[20] which results in a 9 : 1 ratio of T-atoms from the layer structure to Si atoms on linking sites. If all linking sites in the Fe expanded materials were occupied by an Fe atom, this would correspondingly result in a Si/Fe ratio – or (Si+Al)/Fe ratio in case of Al-COE-4/Fe – of 9. According to the elemental analysis results (Table 2) the Fe expanded materials contain enough Fe to occupy around 6% of the linking sites. However, full occupation of the linking sites is not required for a stable material.[30]

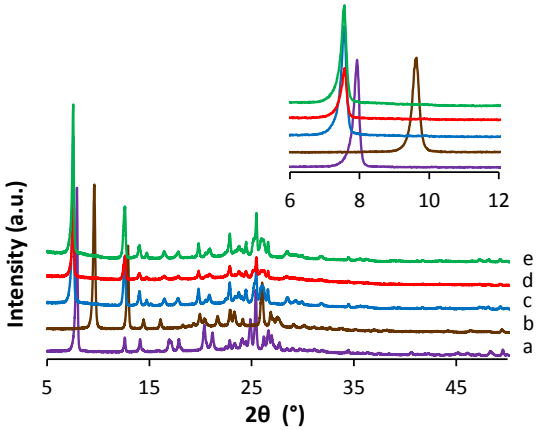

Fig. 1 Powder XRD patterns (Cu $K\alpha_1$ radiation, λ = 1.54056 Å) of RUB-36 (a), RUB-37 (b), Al-COE-4 (c), COE-4/Fe (d) and Al-COE-4/Fe (e). The inset shows a detail of the low angle region for the respective patterns.

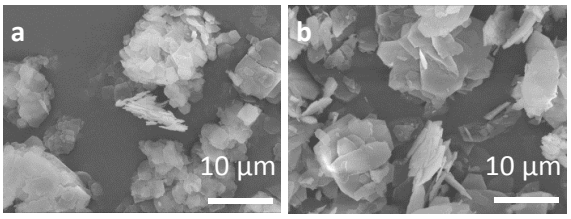

Fig. 2 SEM pictures of COE-4/Fe (a) and Al-COE-4/Fe (b).

An interlayer expansion treatment of RUB-36 in absence of a silylating agent or of the Fe salt can also lead to a shift of the first reflection, in which case the layers are separated by Si atoms from Si debris, resulting in the clear detection of Q^2 Si-species in ^{29}Si MAS NMR.[30] However, there are several structural differences between the material expanded via acid treatment only and the DCDMS or Fe-expanded materials. For instance, the material expanded by acid treatment only is significantly less crystalline, with a diffraction pattern that also shows different features in the higher angle region compared to the DCDMS expanded COE-4 or the Fe-expanded material (Fig. S1). Moreover, the ^{29}Si MAS NMR spectra (Fig. 3) show clearly distinct features for Fe-expanded materials in comparison with materials obtained by acid treatment only. In addition to a strong Q^3 $Si(OSi)_3OH$ signal at -102 ppm due to a large amount of defects, *i.e.* unoccupied linking sites, the material from acid treatment only shows a small signal at -91 ppm, corresponding to Q^2 Si species linking the layers.[20] This assignment is confirmed by the strong enhancement of the signal in the CP spectrum. In the series formed by: acid-only treated material → COE-4/Fe → Al-COE-4/Fe, the Fe-content (Table 2) increases whereas the signal at -91 ppm decreases, especially in the CP spectra. As a $Si((OSi)_3,OFe)$ type species would be expected to overlap with the signal from Q^3 species,[31] the most plausible assignment of this -91 ppm signal, also in the Fe-containing samples, is a Q^2 species. This again suggests that in the presence of Fe, the linking sites are additionally and even preferentially occupied by Fe^{3+} rather than by $Si(OH)_2$ alone. Further interpretation of the CP spectra of the Fe-containing materials should be done with care, since the Fe^{3+} definitely influences the relaxation times.

Table 2 Elemental analysis by ICP-OES and acid properties as determined by FTIR analysis with pyridine as probe molecule.

Sample	Fe (wt.%) [a]	Cl (wt.%) [a]	Si/Fe [a]	Si/Al [a]	BAS (µmol g^{-1}) [b]	LAS (µmol g^{-1}) [b]
Al-COE-4	-	-	-	202	15	10
COE-4/Fe	0.50	<0.01	164	-	4	21
Al-COE-4/Fe	0.56	<0.01	151	148	23	32
Fe_2O_3-ZSM-5	0.45	-	194	57	-	-

[a] Determined from ICP-OES. [b] Number of Brønsted acid sites (BAS) and Lewis acid sites (LAS) determined from the IR absorption bands of chemisorbed pyridine at 150°C.

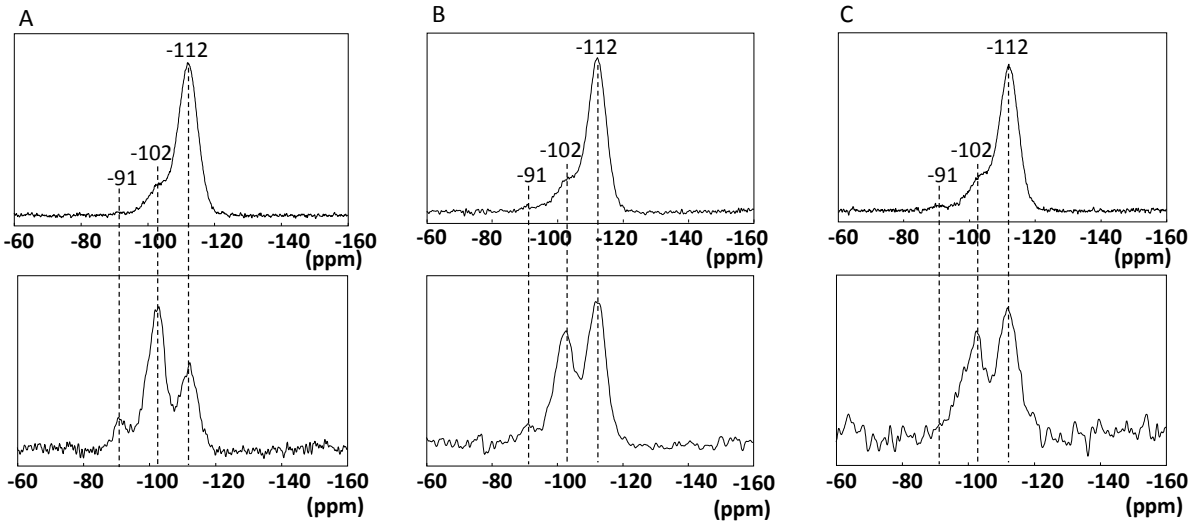

Fig. 3 Single pulse (top) and H-CP ^{29}Si MAS NMR spectra (bottom) of RUB-36 interlayer expanded without the use of a silylating agent or other salt (A), COE-4/Fe (B) and Al-COE-4 (C).

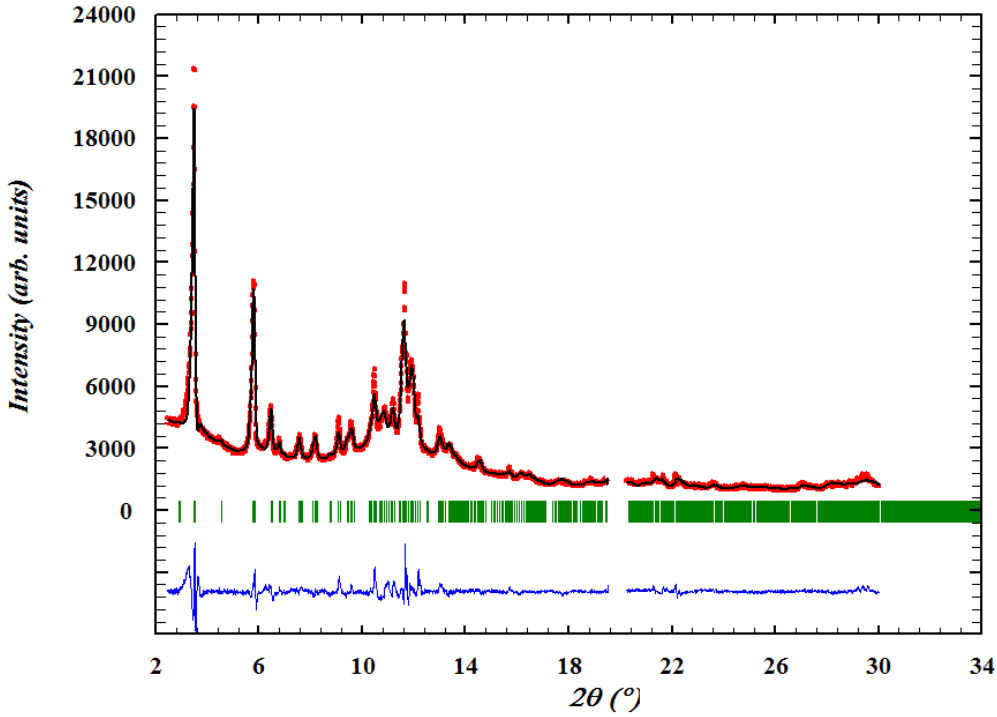

Fig. 4 Result of the Rietveld analysis of COE-3/Fe (χ^2 = 8.75). Experimental (red) and calculated (black) powder XRD pattern of COE-3/Fe (Mo Kα, λ = 0.7106 Å) and the difference plot (blue) are shown.

Structure analysis was performed on the non-calcined material COE-3/Fe (Tables S1-S3). The indexing of the powder diagram yielded the following lattice parameters: *a* = 12.200 Å, *b* = 13.981 Å, *c* = 7.369 Å, *β* = 106.93° (Fig. 4, Table S1). The analysis indicates the presence of increased electron density on the linking sites between the layers, supporting the idea of Fe as linking entity (Fig. 5). Refinement of the structure model shows that the topology of COE-3/Fe is correct and that the linker position contains scatterers stronger than Si alone. Therefore, the siting of the Fe is most likely at the linker position.

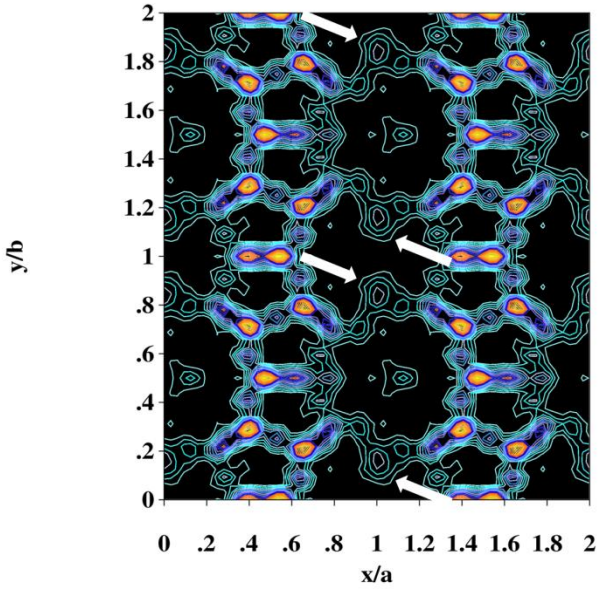

Fig. 5 The electron distribution map of COE-3/Fe showing iso-lines of electron density. This map was obtained from the experimental powder data set by applying a Fourier transform to the structure factors using signs from the structure model as reported. A projection of a segment of the unit cell is shown parallel to the channel axis. The colour code indicates high electron density in yellow as a result of superposition of two or more T- or O-framework atoms. The green colour indicating the linker site (white arrows) and the extra framework atoms (EFA) represents lower electron density due to single occupancies.

Coordination environment of the incorporated iron

To confirm that the Fe is indeed incorporated at isolated sites and not as small Fe-clusters that would not be detected in the XRD because of their size, UV-vis spectra were recorded (Fig. 6). As expected from their respective colors, COE-4/Fe and Al-COE-4/Fe show a UV-vis spectrum that is dramatically different from that of Fe_2O_3-ZSM-5. COE-4/Fe and Al-COE-4/Fe show a clear oxygen-to-metal charge-transfer (CT) band at 259 nm and 268 nm, respectively. Similar spectra have been reported for other Fe-zeolites with isomorphous substitution of Fe in framework positions.[32,33] These bands below 300 nm can be assigned to isolated Fe^{3+} species.[34,35] They cannot unequivocally be related to either tetrahedrally or octahedrallycoordinated Fe^{3+} as these both have transitions in the same energy range.[34] Oligomeric Fe-clusters and larger Fe-oxide aggregates are expected to show CT bands between 300 and 400 nm and at larger wavelengths, respectively,[32,34,35] but these bands are not observed for the COE-4 type materials. Fe_2O_3-ZSM-5 on the other hand, has a very broad absorption spectrum that extends well beyond 300 nm. This clearly indicates the presence of a variety of Fe-oxide species, smaller and larger ones, with overlapping absorption bands.[35] A weak *d-d* transition can be observed for COE-4/Fe at 442 nm and for Al-COE-4/Fe at 426 nm. However, only one *d-d* transition is observed and because the Tanabe and Sugano diagrams for the octahedral and tetrahedral coordination are

similar, this band alone does not allow to draw conclusions regarding the exact environment of the incorporated Fe.[34,36] In any case, it can be concluded from the UV-Vis spectra that the Fe in the COE-4-type materials consists mainly of isolated Fe^{3+} species coordinated by oxygen atoms, in a tetrahedral and/or octahedral coordination.

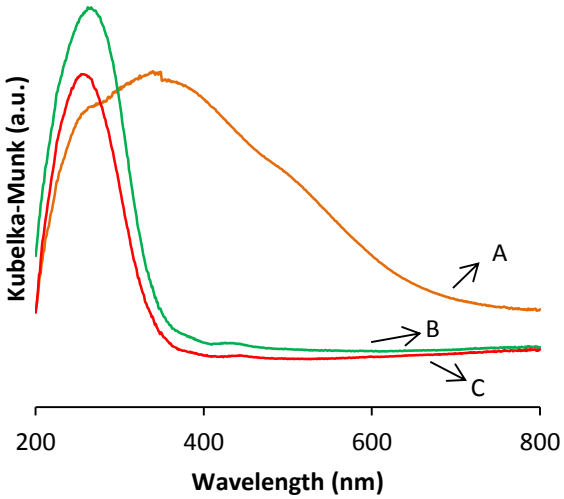

Fig. 6 UV-vis spectra of Fe_2O_3-ZSM-5 (A), Al-COE-4/Fe (B), and COE-4/Fe (C).

The coordination state of the incorporated Fe was also investigated using EPR (Fig. 7). The EPR signals of Fe containing zeolitic materials strongly depend on the zero field splitting parameters *D* and *E*. The latter are closely related to the local crystal field symmetry and reflect the departure from a highly symmetric coordination.[34,35] Signals at $g \approx 4.3$ and $g \approx 2.0$ are often observed, but their interpretation is not straightforward. Usually, the signal at $g \approx 4.3$ is assigned to Fe^{3+} ions in a distorted tetrahedral coordination, though not necessarily in framework positions.[37] It can however also correspond to a strongly distorted octahedral coordination. The signal at $g \approx 2.0$ can be ascribed to isolated Fe^{3+} in a more symmetric environment with $D, E \approx 0$. Small Fe oxide clusters can also contribute to this signal due to magnetic interactions between the Fe^{3+} ions, which average out the zero field splitting.[35] Clear signals at $g \approx 4.3$ and $g \approx 2.0$ can be observed for both Fe_2O_3-ZSM-5 and Al-COE-4/Fe, but their behavior upon removing the adsorbed water and upon variation of the measurement temperature is different. Al-COE-4/Fe (Fig. 7b) shows an increase of the signal at $g \approx 4.3$ upon dehydration whereas the signal at $g \approx 2.0$ decreases, as shown by spectra at 116 K. This is an indication that the signal at $g \approx 2.0$ corresponds more likely to isolated Fe^{3+} sites, of which the coordination number is reduced or the coordination sphere distorted upon dehydration, than to Fe oxide particles. The signal intensity at $g \approx 2.0$ is also reduced upon increasing the measurement temperature. This Curie-law behavior ($I \sim 1/T$) is expected for highly symmetric, isolated Fe^{3+} species.[35] Fe_2O_3-ZSM-5 also shows a signal at $g \approx 2.0$ but it is a broader signal and its intensity increases with temperature. According to Kumar *et al.*[35] this is caused by antiferromagnetic interactions which collapse upon increasing the measurement temperature; thus the signal can be ascribed to neighboring Fe^{3+} species in small Fe oxide clusters. These results are consistent with the UV-vis spectra and also indicate that Al-COE-4/Fe contains mostly isolated Fe species (tetrahedral and/or octahedral).

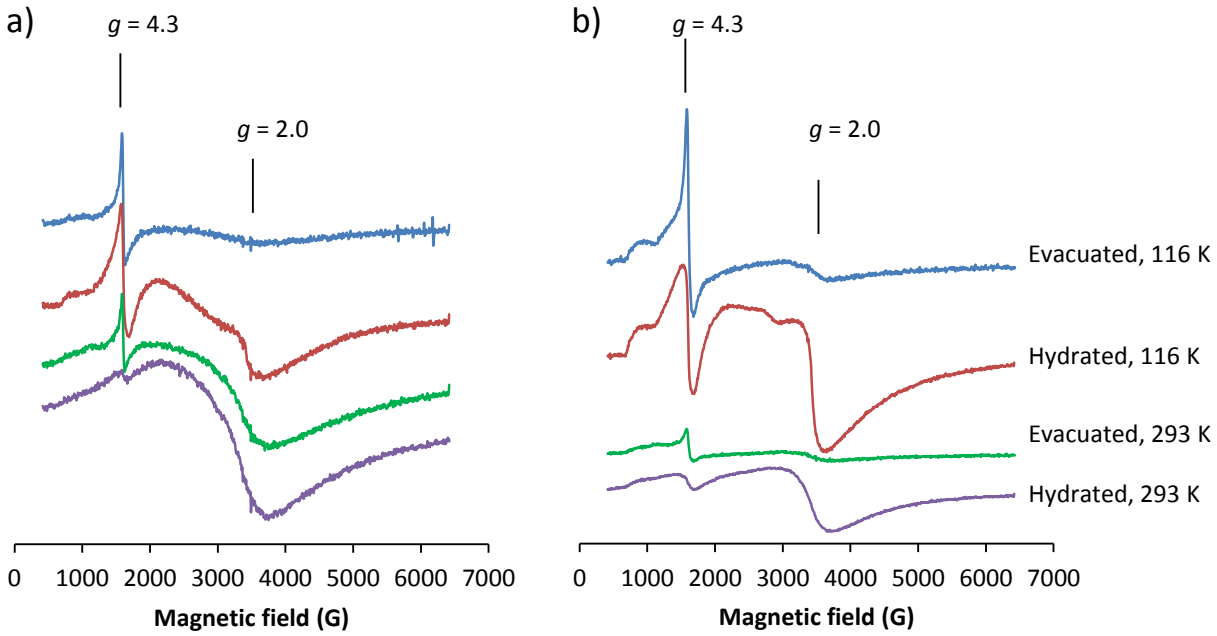

Fig. 7 EPR spectra of Fe_2O_3-ZSM-5 (a) and (Al)-COE-4/Fe (b) obtained at 116K and 293K (9.600 GHz). Spectra were collected before dehydration under ambient conditions and under N_2 atmosphere after evacuation.

Acidity characterization

The acidity of the different COE-4-type materials was characterized with FTIR analysis using various probe molecules. Using pyridine as probe molecule, the presence of Brønsted and Lewis acid sites and their relative contribution can be determined. The difference spectra after adsorption of pyridine are shown in Fig. 8. In Al-COE-4, pyridine is adsorbed on mainly Brønsted acid sites (1543 cm^{-1}), with only a minor fraction on Lewis acid sites (1452 cm^{-1}). COE-4/Fe on the other hand shows a large number of pyridine molecules interacting with Lewis acid sites. When an Al-containing layered precursor is used as in Al-COE-4/Fe, an even higher number of Lewis acid sites is obtained, resulting mostly from the incorporated Fe, but also a fair contribution of Brønsted acid sites from the Al in the precursor layer can be seen (Table 2).

To demonstrate the difference between the Al and Fe related Lewis acid sites, the adsorption of acetonitrile on the COE-4 type materials was investigated. Acetonitrile is a smaller probe molecule and a weaker base than pyridine; it sometimes can be used to obtain a better resolution in detecting Lewis acid sites.[38] Upon interaction with Lewis acid sites, the C≡N stretching vibration is perturbed. The shift of the vibrational frequency is more pronounced with a larger charge transfer from the probe molecule to the acid site. Liquid acetonitrile has a doublet at 2294 and 2254 cm^{-1} resulting from the Fermi resonance between the ν(C≡N) and the (ν(C-C) + $\delta_s(CH_3)$) combination mode. After adsorption, both peaks shift upwards due to electron withdrawal from the N lone pair.[38-40] In the spectra of all three COE-4 type materials, this doublet is observed at 2297 and 2266 cm^{-1} (Fig. 9). These absorption bands are well known to arise from the interaction of the acetonitrile with OH groups via hydrogen bonds.[40,41] For the Fe-containing materials, an additional strong absorption band of acetonitrile is observed at 2315 cm^{-1}. This band is not observed on Al-COE-4 and can be safely assigned to an interaction of acetonitrile with the Lewis acid sites originating from the incorporated Fe. The spectrum of Al-COE-4 has an additional, very weak absorption band at 2334 cm^{-1}. This can be assigned to the presence of a small amount of Lewis acid sites,[41] the presence of which was also inferred from the adsorption of pyridine (Fig. 8). The band also appears as a small shoulder on the left side

from the 2315 cm^{-1} band of the Al-COE-4/Fe spectrum but could not be detected for COE-4/Fe. Therefore this absorption band was assigned to Al related Lewis acid sites.

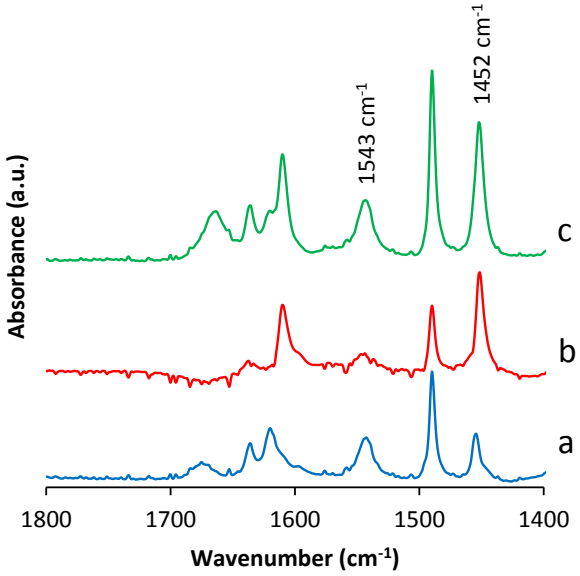

Fig. 8 Difference IR spectra (at 423 K) of adsorbed pyridine on Al-COE-4 (a), COE-4/Fe (b) and Al-COE-4/Fe (c) normalized to 10 mg cm^{-2}. The absorption bands at 1455-1450 cm^{-1} and 1550-1545 cm^{-1} correspond to pyridine adsorbed on Lewis resp. Brønsted acid sites.

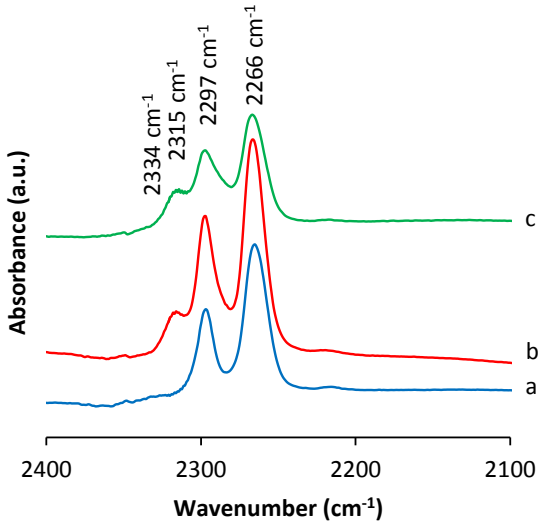

Fig. 9 C≡N stretching region of the difference IR spectra (at 298 K) of adsorbed acetonitrile on Al-COE-4 (a), COE-4/Fe (b) and Al-COE-4/Fe (c) normalized to 10 mg cm^{-2}.

When perdeuterated acetonitrile is used as probe molecule (Fig. 10), the Fermi resonance doublet disappears and only one band at 2276 cm^{-1} remains. With this probe as well, the Fe-containing materials show an additional absorption band at 2305 cm^{-1} which is not observed on Al-COE-4 and can again be assigned to the interaction of the perdeuterated acetonitrile with Fe Lewis acid sites. Al-COE-4 displays a minor absorption band at 2325 cm^{-1}, which was also observed on Al-COE-4/Fe and is assigned to the interaction with Al related Lewis acid sites.[42,43]

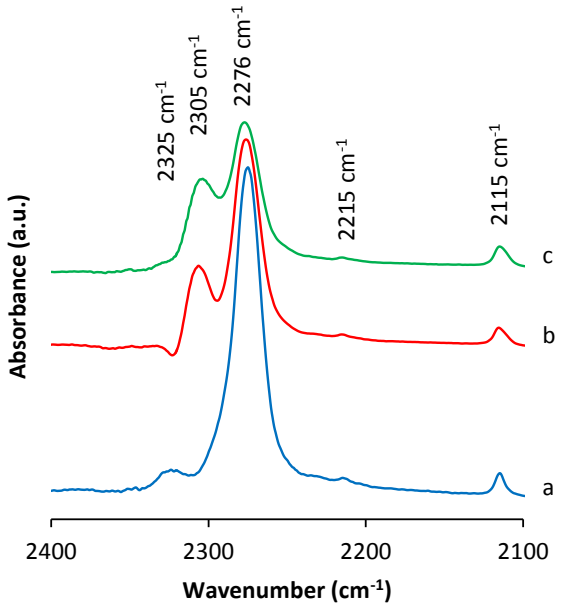

Fig. 10 C≡N stretching region of the difference IR spectra (at 298 K) of adsorbed perdeuterated acetonitrile on Al-COE-4 (a), COE-4/Fe (b) and Al-COE-4/Fe (c) normalized to 10 mg cm^{-2}.

Catalytic activity and stability

Catalytic activity of the Fe expanded materials was investigated in acylation and alkylation reactions. In the acylation of anisole with acetic anhydride (Table 3, Figure S2), *p*-methoxyacetophenone (*p*MAP) was the main product (selectivity based on anisole > 98%) with a minor formation of o-methoxyacetophenone. Comparison of the yields and turn-over numbers (TON) shows that Al-COE-4/Fe is more active than DCDMS expanded Al-COE-4.

Table 3 Catalytic activity of Al-COE-4 and Al-COE-4/Fe in the acylation of anisole with acetic anhydride.

Catalyst	*p*MAP yield (%)[a]	TON[a,b]
Al-COE-4	2	30
Al-COE-4/Fe	12	55

[a] After 1 h of reaction, based on acetic anhydride. [b] TON in mol(acetic anhydride)/mol(Al^{3+}+Fe^{3+}).

Alkylation of toluene with benzylchloride was also used as a test reaction for the Fe-containing catalysts. It has been shown in previous studies[24,44] that reducible cations, such as Fe^{3+}, have a beneficial effect on the activity in this type of reaction. In the proposed reaction mechanism[44] the initiation of the reaction involves a radical step in which the homolysis of the carbon-chlorine bond is triggered by the reduction of Fe^{3+} (Scheme 1). The benzyl carbocation then takes part in the electrophilic aromatic substitution and the formed Fe^{2+} is returned to its Fe^{3+} state by reduction of the chlorine radical to chloride.

$$Ph\text{-}CH_2Cl + Fe^{3+} \rightarrow Ph\text{-}CH_2^{+} + Cl^{\cdot} + Fe^{2+}$$

$$Fe^{2+} + Cl^{\cdot} \rightarrow Fe^{3+} + Cl^{-}$$

Scheme 1 Carbocation formation from benzyl chloride, as catalyzed by Fe^{3+} species.

As can be seen from Fig. 11, the aluminosilicate Al-COE-4 itself is not capable of performing the alkylation under these reaction conditions. After incorporation of Fe, both COE-4/Fe and Al-COE-4/Fe show almost full conversion after 24 h. The change of color from white to green of the Fe expanded materials and the lack of activity of Al-COE-4 confirm the aforementioned reaction mechanism. Also the UV-vis spectrum of Al-COE-4/Fe indicates a change of the state of the incorporated Fe after reaction (Fig. S3). When the iron is deposited in the zeolite, such as in Fe_2O_3-ZSM-5, the HCl, which is a stoichiometric by-product of the reaction, is troublesome regarding the heterogeneity and stability of the Fe in the catalyst. Therefore, both leaching tests and catalyst regeneration tests were performed. As can be seen from Fig. 12, when the Fe_2O_3-ZSM-5 catalyst is removed from the reaction mixture after only 3 min, the reaction still proceeds and full benzyl chloride conversion was reached after 24 h. The COE-4 type materials on the other hand, do not leach catalytically active Fe-species. It is however possible that catalytically inactive Fe species leach, as has been observed for the mesoporous Fe-containing silica materials.[45,46] To exclude this possibility, elemental analysis of the catalyst after reaction was performed. For Fe_2O_3-ZSM-5, the Si/Fe ratio increased from 194 before reaction to 283 after reaction, indicating that around 30% of the Fe has leached. In Al-COE-4/Fe (Si/Fe 151) on the other hand, the Si/Fe ratio remains similar after reaction (Si/Fe 149). This proves that because of the interlayer expansion treatment, the Fe incorporation into the COE-4 material is much more stable than for impregnated Fe oxide particles. The possibility to reuse the Al-COE-4/Fe was also explored. After regeneration via a simple calcination procedure, Al-COE-4/Fe shows a slightly lower activity than the fresh catalyst but almost full conversion of benzylchloride is still reached after 24h (Fig. S4).

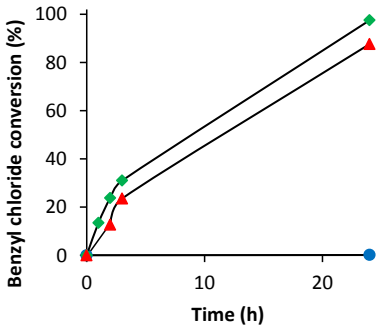

Fig. 11 Benzyl chloride conversion in the benzylation of toluene at 343 K for Al-COE-4 (●), COE-4/Fe (▲), and Al-COE-4/Fe (♦).

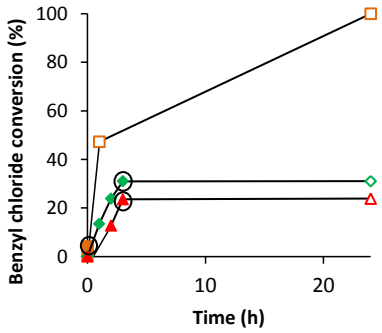

Fig. 12 Filtration tests in the benzylation of toluene for COE-4/Fe (▲/△), Al-COE-4/Fe (◆/◇) and Fe_2O_3-ZSM-5 (■/□). The last data points right before removing the catalysts are indicated with a circle. Open symbols represent the conversion after the catalyst was removed.

Conclusions

Incorporation of Lewis acid sites was achieved via an interlayer expansion treatment of RUB-36 using Fe chloride instead of a silylating agent. The obtained material showed a similar expansion of the precursor layers as after interlayer expansion with DCDMS. Different characterization techniques (elemental analysis, UV-Vis, EPR, FT-IR) allowed us to conclude that the Fe was incorporated as isolated Fe^{3+} species exhibiting Lewis acid properties. The results of acylation and alkylation reactions indicate that the interlayer expansion treatment with Fe chloride can be used as an alternative route to obtain active and stable catalysts from layered zeolite precursors and could lead to methods for introducing other metals at well-defined sites in zeolitic materials. The concept of heteroatom pillaring constitutes a novel platform to incorporate catalytically active centers into silicate frameworks, which would allow design of active sites at an atomic level. With their unique composition, structure and pore architecture, these novel zeolitic materials offer significant promise in industrial catalysis.

Acknowledgements

The authors would like to thank Dr. K. Houthoofd for collecting the NMR spectra. T.D.B. acknowledges F.W.O. – Vlaanderen (Research Foundation – Flanders) for a doctoral fellowship. D.E.D.V. thanks Belspo (IAP 7/05) and KU Leuven (CASAS Metusalem grant). Support of BASF SE under the INCOE framework is acknowledged.

Notes and references

[a] Centre for Surface Chemistry and Catalysis, KU Leuven, Kasteelpark Arenberg 23, Post Box 2461, 3001, Leuven, Belgium. E-mail: Dirk.DeVos@biw.kuleuven.be.

[b] Institute of Geology, Mineralogy and Geophysics, Ruhr-University Bochum, 44780, Bochum, Germany.

[c] BASF Corporation, Chemicals Research and Engineering, Iselin, NJ 08830, USA.

[d] BASF SE, Chemicals Research and Engineering, 67056, Ludwigshafen, Germany.

[e] Zhejiang University, 310028, Hangzhou, China.

[f] State Key Laboratory of Fine Chemicals, Dalian University of Technology, 116024, Dalian, China.

[g] Chemical Resources Laboratory, Tokyo Institute of Technology, 226-8503, Yokohama, Japan.

[h] State Key Laboratory of Catalysis, Dalian Institute of Chemical Physics, 116023, Dalian, China.

† Electronic Supplementary Information (ESI) available: [additional experimental information, structure refinement details, characterization and catalytic results]. See DOI: 10.1039/c4ta01384k

1 B. Yilmaz and U. Müller, *Top. Catal.,* 2009, **52**, 888.

2 C. Martínez and A. Corma, *Coord. Chem. Rev.*, 2011, **255**, 1558.

3 J.A. Martens, M. Tielen, P.A. Jacobs and J. Weitkamp, *Zeolites,* 1984, **4**, 98.

4 B. Yilmaz, U. Müller, M. Feyen, H. Zhang, F.-S. Xiao, T. De Baerdemaeker, B. Tijsebaert, P. Jacobs, D. De Vos, W. Zhang, X. Bao, H. Imai, T. Tatsumi and H. Gies, *Chem. Commun.,* 2012, **48**, 11549.

5 Z. Da, Z. Han, P. Magnoux and M. Guisnet, *Appl. Catal., A,* 2001, **219**, 45.

6 X.-Q. Zhang, T. T. Trinh, R. A. van Santen and A. P. J. Jansen, *J. Am. Chem. Soc.*, 2011, **133**, 6613.

7 X.-Q. Zhang, R. A. van Santen and A. P. J. Jansen, *Phys. Chem. Chem. Phys.*, 2012, **14**, 11969.

8 B. Marler and H. Gies, *Eur. J. Mineral.,* 2012, **24**, 405.

9 S.L. Lawton, A.S. Fung, G.J. Kennedy, L.B. Alemany, C.D. Chang, G.H. Hatzikos, D.N. Lissy, M.K. Rubin, H.-K.C. Timken and S. Steuernagel, *J. Phys. Chem.,* 1996, **100**, 3788.

10 L. Schreyeck, P. Caullet, J. Mougenel, J. Guth and B. Marler, *Microporous Mater.,* 1996, **6**, 259.

11 S. Zanardi, A. Alberti, G. Cruciani, A. Corma, V. Fornes and M. Brunelli, *Angew. Chem., Int. Ed.,* 2004, **43**, 4933.

12 Y. Wang, H. Gies, B. Marler and U. Müller, *Chem. Mater.,* 2005, **17**, 43.

13 R. Millini, G. Perego, W. Parker Jr, G. Bellussi and L. Carluccio, *Microporous Mater.,* 1995, **4**, 221.

14 P. Wu, J. Ruan, L. Wang, L. Wu, Y. Wang, Y. Liu, W. Fan, M. He, O. Terasaki and T. Tatsumi, *J. Am. Chem. Soc.,* 2008, **130**, 8178.

15 Z. Zhao, W. Zhang, P. Ren, X. Han, U. Müller, B. Yilmaz, M. Feyen, H. Gies, F.-S. Xiao, D. De Vos, T. Tatsumi and X. Bao, *Chem. Mater.,* 2013, **25**, 840.

16 A. Corma, V. Fornes, J. Martınez-Triguero and S. Pergher, *J. Catal.,* 1999, **186**, 57.

17 A. Corma, V. Fornes, S. Pergher, T.L. Maesen and J. Buglass, *Nature,* 1998, **396**, 353.

18 S. Maheshwari, E. Jordan, S. Kumar, F.S. Bates, R.L. Penn, D.F. Shantz and M. Tsapatsis, *J. Am. Chem. Soc.,* 2008, **130**, 1507.

19 J. Ruan, P. Wu, B. Slater, Z. Zhao, L. Wu and O. Terasaki, *Chem. Mater.,* 2009, **21**, 2904.

20 H. Gies, U. Müller, B. Yilmaz, M. Feyen, T. Tatsumi, H. Imai, H. Zhang, B. Xie, F.-S. Xiao, X. Bao, W. Zhang, T. De Baerdemaeker and D. De Vos, *Chem. Mater.,* 2012, **24**, 1536.

21 H. Gies, U. Müller, B. Yilmaz, T. Tatsumi, B. Xie, F.-S. Xiao, X. Bao, W. Zhang and D. De Vos, *Chem. Mater.,* 2011, **23**, 2545.

22 B. Tijsebaert, M. Henry, H. Gies, F.-S. Xiao, W. Zhang, X. Bao, H. Imai, T. Tatsumi, U. Müller, B. Yilmaz, P. Jacobs and D. De Vos, *J. Catal.,* 2011, **282**, 47.

23 B. Yilmaz, U. Müller, T. De Baerdemaeker, H. Gies, F.-S. Xiao, T. Tatsumi, X. Bao, W. Zhang and D. De Vos, WIPO Patent 2012001663, 2012.

24 V.R. Choudhary and S.K. Jana, *Appl. Catal., A,* **2002**, *224*, 51-62.

25 C. Baerlocher, A. Hepp and W.M. Meier, DLS-76: A Program for the Simulation of Crystal Structures by Geometric Refinement. http://www.crystal.mat.ethz.ch/Software/DLS76.

26 J. Rodriguez-Carvajal, *J. Physica B,* 1993, 55.

27 J. Rodriguez-Carvajal, FullProf Suite Homepage. http://www.ill.eu/sites/fullprof/.

28 C. Emeis, *J. Catal.,* 1993, **141**, 347.

29 P. Horcajada, S. Surblé, C. Serre, D.-Y. Hong, Y.-K. Seo, T.-S. Chang, J.-M. Grenèche, I. Margiolaki and G. Férey, *Chem. Commun.,* 2007, 2820.

30 T. Ikeda, S. Kayamori, Y Oumi and F. Mizukami, *J. Phys. Chem. C,* 2010, **114**, 3466.

31 V. Umamaheswari, W. Böhlmann, A. Pöppl, A. Vinu, and M. Hartmann, *Microporous Mesoporous Mater.,* 2006, **89**, 47.

32 E. Hensen, Q. Zhu, R. Janssen, P. Magusin, P. Kooyman and R. Van Santen, *J. Catal.,* 2005, **233**, 123.

33 J. Pérez-Ramírez, J. Groen, A. Brückner, M.S. Kumar, U. Bentrup, M. Debbagh and L. Villaescusa, *J. Catal.,* 2005, **232**, 318.

34 S. Bordiga, R. Buzzoni, F. Geobaldo, C. Lamberti, E. Giamello, A. Zecchina, G. Leofanti, G. Petrini, G. Tozzola and G. Vlaic, *J. Catal.,* 1996, **158**, 486.

35 M.S. Kumar, M. Schwidder, W. Grünert and A. Brückner, *J. Catal.,* 2004, **227**, 384.

36 D. Arieli, D. Vaughan, K. Strohmaier, H. Thomann, M. Bernardo and D. Goldfarb, *Magn. Reson. Chem.,* 1999, **37**, S43.

37 P. Fejes, I. Kiricsi, K. Lázár, I. Marsi, A. Rockenbauer, L. Korecz, J.B. Nagy, R. Aiello and F. Testa, *Appl. Catal. A: Gen.,* 2003, **242**, 247.

38 G. Busca, *Phys. Chem. Chem. Phys.,* 1999, **1**, 723.

39 J. Fernández Bertrán, B. La Serna, K. Doerffel, K. Dathe and G. Kabish, *J. Mol. Struct.,* 1982, **95**, 1.

40 A. Travert, A. Vimont, J.-C. Lavalley, V. Montouillout, M. Rodriguez Delgado and J. Cuart Pascual, C. Otero Areán, *J. Phys. Chem. B,* 2004, **108**, 16499.

41 O. Marie, F. Thibault-Starzyk and J.-C. Lavalley, *Phys. Chem. Chem. Phys.,* 2000, **2**, 5341.

42 O. Bortnovsky, Z. Melichar, Z. Sobalík and B. Wichterlová, *Microporous Mesoporous Mater.,* 2001, **42**, 97.

43 B. Wichterlová, Z. Tvarůžková, Z. Sobalık and P. Sarv, *Microporous Mesoporous Mater.,* 1998, **24**, 223.

44 T. Cseri, S. Békássy, F. Figueras and S. Rizner, *J. Mol. Catal. A: Chem.,* 1995, **98**, 101.

45 A. Arafat and Y. Alhamed, *J. Porous Mater.,* 2009, **16**, 565.

46 M. Hamdy, G. Mul, J. Jansen, A. Ebaid, Z. Shan, A. Overweg and T. Maschmeyer, *Catal. Today,* 2005, **100**, 255.